JGR Oceans

Key Points:
- Observational evidence demonstrates the signature of near-inertial wave trapping near the base of a mesoscale anticyclonic eddy during low to moderate wind conditions
- The trapped near-inertial waves produce low fine-scale Richardson numbers and enhanced strain variance, suggesting turbulence production
- Enhanced vertical mixing may presumably be found inside similar open-ocean eddies under normal atmospheric conditions

Correspondence to:
A. Martínez-Marrero,
antonio.martinez@ulpgc.es

Near-Inertial Wave Trapping Near the Base of an Anticyclonic Mesoscale Eddy Under Normal Atmospheric Conditions

A. Martínez-Marrero[1] (iD), B. Barceló-Llull[2] (iD), E. Pallàs-Sanz[3] (iD), B. Aguiar-González[4] (iD), S. N. Estrada-Allis[3] (iD), C. Gordo[1] (iD), D. Grisolía[1], A. Rodríguez-Santana[4] (iD), and J. Arístegui[1] (iD)

[1]Instituto de Oceanografía y Cambio Global (IOCAG), Universidad de Las Palmas de Gran Canaria (ULPGC) Unidad Asociada ULPGC-CSIC, Las Palmas de Gran Canaria, Spain, [2]Applied Physics Laboratory, University of Washington, Seattle, WA, USA, [3]Departamento de Oceanografía Física, CICESE, Ensenada, México, [4]Departamento de Física, Universidad de Las Palmas de Gran Canaria (ULPGC), Las Palmas de Gran Canaria, Spain

Abstract Observational evidence demonstrates the signature of near-inertial wave (NIW) trapping by a long-lived westward propagating mesoscale anticyclonic eddy under normal atmospheric conditions. Cross-eddy sections of density and shipboard acoustic Doppler current profiler data show the downward (upward phase) propagation of NIW packets with vertical wavelengths of 200 m within the eddy, and wave energy amplification in a critical vertical layer located near the base of the anticyclone. Elevated strain variance, enhanced turbulent kinetic energy dissipation rates obtained from a fine-scale parameterization, and the occurrence of low (≤ 1) gradient Richardson numbers are consistent with turbulence production and mixing from 400 m to at least the maximum sampling depth of 725 m associated with the trapped NIWs. The observation of NIW packets near the eddy base at two different stages of the survey separated by 10 days and the persistence of low to moderate winds before and during the eddy sampling strongly suggest that our findings may be common in similar open-ocean anticyclonic eddies under normal wind conditions.

Plain Language Summary Near-inertial waves—or internal gravity waves with a frequency near the inertial frequency—are typically excited at the sea surface by variable wind stress forcing. These waves can be trapped and amplified at the base of mesoscale (horizontal scales of about 10–100 km) anticyclonic eddies, especially after storms or strong wind events, situations in which high near-inertial energy is generated. In this article we present observational evidence of near-inertial wave trapping during low to moderate wind conditions. We also show that these trapped waves lead to deep mixing near the base of the eddy. The observation of near-inertial wave packets on two different dates and the low to moderate winds persistent during the survey suggest that our findings may be common in other similar open-ocean eddies. Mesoscale anticyclonic eddies of the World Ocean may therefore act as deep mixing structures as they propagate westward.

1. Introduction

An increasing number of studies support the idea that internal waves are largely responsible for the deep small-scale mixing that is necessary to increase interior ocean water mass potential energy (e.g., Alford, 2003; Munk & Wunsch, 1998; Waterhouse et al., 2014; Whalen et al., 2012; Wunsch & Ferrari, 2004). The main sources of internal waves are internal tides produced by topographic interactions (St. Laurent & Garrett, 2002) and near-inertial waves (NIWs), which are typically excited within the sea surface mixed layer by variable wind stress forcing (D'Asaro et al., 1995; Pollard & Millard, 1970). As NIWs are ubiquitous features of the World Ocean, they are suggested to play a significant role in deep small-scale mixing (Alford et al., 2016). In this regard the key issue is what, and how effective, are the mechanisms by which wind-generated NIWs propagate downward and dissipate their energy and thus induce small-scale deep mixing. The β-dispersion effect, which produces both downward and equatorward propagation, has been proposed as a first candidate (e.g., Anderson & Gill, 1979; Garrett, 2001). Alternatively, Kunze (1985) posited that a region of negative (anticyclonic) relative vorticity, such as an anticyclonic eddy, increases the vertical group velocity of NIWs entering from the outside and, at the same time, may trap NIWs excited by the wind inside the region.

Kunze's (1985) approach relies on the concept of the effective Coriolis frequency, or lowest bound of the internal wave frequency band, $f_{\text{eff}} = f + \zeta/2$, where f is the local Coriolis frequency and ζ is the background relative vorticity. When NIWs are excited inside a region of anticyclonic relative vorticity, they can have frequencies below f and thus remain trapped as they cannot propagate out of the rotating region. Moreover, NIWs are trapped not only in the horizontal but also at critical layers in the vertical. As the waves travel downward from the surface, they reflect off the sides of the anticyclonic region (turning points) and then stall within a critical layer at the base of the anticyclonic vorticity region, where the group velocity drops to 0. When the NIWs approach this critical layer, their amplitude must grow, their vertical wavelengths shrink, and the vertical shear and nonlinear effects are eventually able to extract and dissipate the waves' energy, enabling the production of turbulence and associated deep small-scale vertical mixing (Kunze et al., 1995).

The initial horizontal scales of NIWs at the surface are much larger than the scales of mesoscale eddies, which violates the assumption of the Wentzel-Kramers-Brillouin approach used by Kunze (1985). Young and Ben Jelloul (1997) and Balmforth et al. (1998) introduced a different but complementary approach that avoids the horizontal scale assumption implicit in the Wentzel-Kramers-Brillouin approximation. Their results show that the vorticity associated with a geostrophic eddy field essentially distorts the large-scale near-inertial motions at eddy length scales, which subsequently allow them to propagate more rapidly downward. More recently, Whitt and Thomas (2012) theoretically investigated this process for the case of strong baroclinicity and showed that NIWs can be trapped inside negative vorticity regions on slantwise critical layers that align with the tilted isopycnals.

Following the above theoretical approaches, several numerical process-oriented studies have been conducted to investigate the trapping of NIWs by mesoscale eddies (e.g., Danioux et al., 2015; Danioux & Klein, 2008; Joyce et al., 2013; Lee & Niiler, 1998; Zhai et al., 2005, 2007). Their results support the theoretical predictions showing that mesoscale anticyclonic eddy fields drain near-inertial energy from the ocean surface to the deep layers. Lee and Niiler (1998) called this effect the "inertial chimney effect." However, observations of this inertial chimney effect in mesoscale anticyclonic eddies are scarce and incomplete (Alford et al., 2016). Microstructure measurements from large Gulf Stream rings (Kunze et al., 1995; Lueck & Osborn, 1986) show elevated turbulent dissipation rates (ϵ) at the ring core bases of up to 2 orders of magnitude higher than their surroundings. Cuypers et al. (2012) observed ϵ of $O(10^{-8})$W/kg and large near-inertial vertical shear values at the base of eddies in the Mediterranean Sea. Joyce et al. (2013), using direct velocity measurements, obtained in situ observations of a trapped near-inertial mode at the base of a large Gulf Stream warm-core ring after a storm. Pallàs-Sanz et al., 2016, Pallàs-Sanz et al., 2016) observed hurricane-induced near-inertial energy packets traveling with mean vertical group velocities of 60–70 m/day toward the base of the Loop Current and a region of anticyclonic vorticity in the Gulf of Mexico. More recent microstructure studies have reported enhanced diapycnal mixing (ϵ of $O(10^{-8})$W/kg) below an anticyclonic eddy in the Arctic Ocean after a rapidly moving storm had passed (Kawaguchi et al., 2016) and also below the core of a long-lived eddy in the Norwegian Sea (Fer et al., 2018). Karstensen et al. (2017) observed NIWs of ± 0.1-m/s amplitude and 80- to 100-m vertical wavelength beneath an anticyclonic intrathermocline eddy that they attributed to NIW trapping.

Most of the above observations were obtained in the cores of intense eddies associated with western boundary currents or after strong wind events, situations in which high near-inertial energy is generated. However, sea surface height maps have confirmed that mesoscale variability is dominated by a large number of westward propagating eddies of moderate amplitude throughout most of the World Ocean (Chelton et al., 2007). Additional results obtained by Chelton et al. (2011) showed that eddy formation rates are highest in the eastern boundary current regions and that anticyclonic eddies have preferentially long lifetimes (≥ 16 weeks) and propagate over longer distances than cyclonic eddies. Due to the ubiquity of these features in the World Ocean, the trapping of NIWs within long-lived westward propagating anticyclonic eddies under moderate wind forcing conditions may become an important source of interior ocean vertical mixing. To our knowledge, NIW trapping by average eddies under moderate wind conditions has not yet been demonstrated with observational data.

In September 2014 we conducted an interdisciplinary survey of an anticyclonic eddy within the framework of the PUMP (Study of the Vertical Oceanic Pump in mesoscale eddies) experiment (Barceló-Llull et al.,
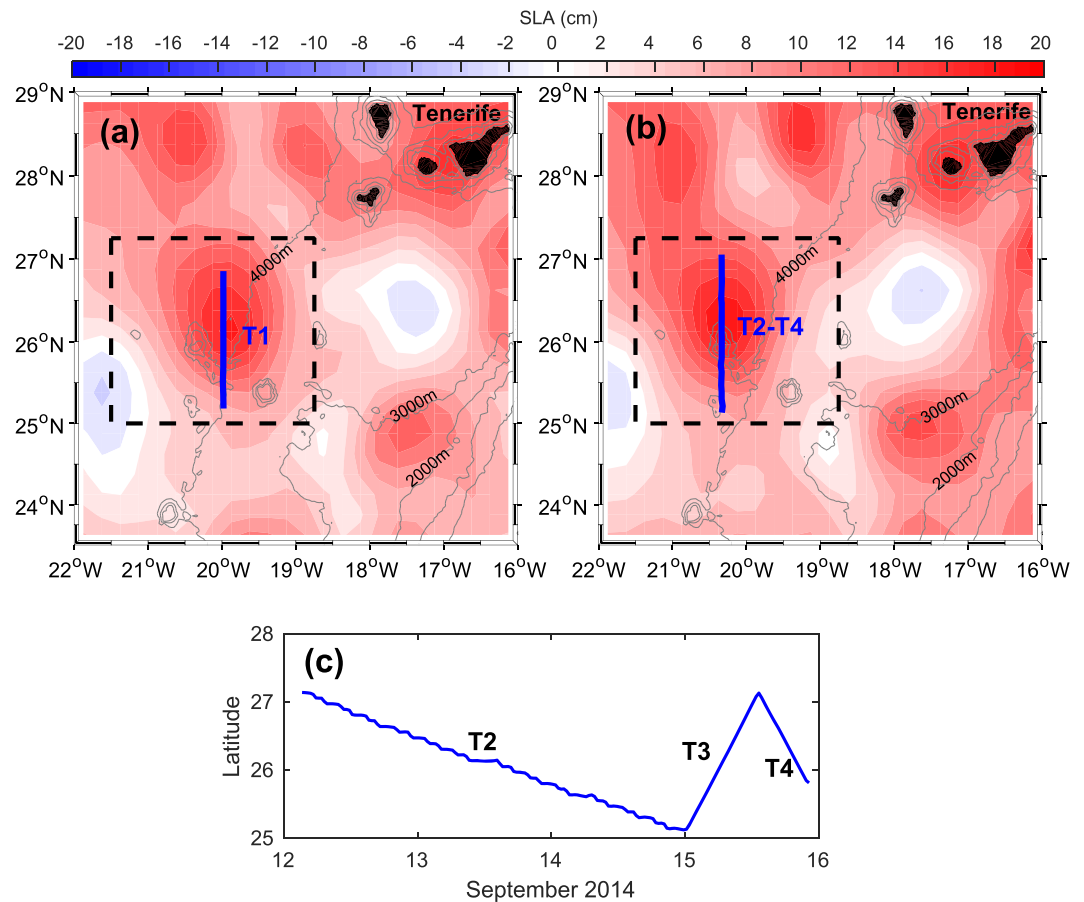
Figure 1. Location of the four transects sampled during the PUMP oceanographic survey: (a) sea level anomaly (SLA) on 4 September 2014 with bathymetry in gray contours. The blue line indicates the first transect (T1) carried out on this day to obtain underway SADCP data across the eddy. Dashed black rectangle marks the area used to obtain mean winds from the ASCAT scatterometer of the MetOp-A satellite (http://marine.copernicus.eu/). (b) Sea level anomaly on 14 September. The blue line shows the location of Transects 2 (T2), 3 (T3), and 4 (T4) carried out between 12 and 16 September to obtain CTD and SADCP data. (c) Temporal and spatial sampling of transects T2–T4. T2 was carried out with stops every 5 nm for CTD casts and repeated two more times (T3 and T4) without stopping, recording only SADCP data.

2017). The eddy was located inside the so-called Canary Eddy Corridor, southwest of the Canary Islands, which is a major pathway for long-lived mesoscale eddies in the northeast subtropical Atlantic (Sangrà et al., 2009). One of the main goals of the experiment was to test, by means of high-resolution field observations, if under nonextraordinary wind forcing conditions, an open-ocean mesoscale anticyclonic eddy can trap NIWs and thus provide energy for deep turbulent mixing.

2. Data

The oceanographic PUMP survey was carried out aboard the R/V *BIO Hespérides* from 31 August to 23 September 2014, the time of the year the area has weakest winds (Barceló-Llull et al., 2017). The sampled eddy was generated through the interaction of the Canary Current with the island of Tenerife 4 months before the cruise and was tracked with gridded altimetry data, provided by AVISO (http://www.aviso.altime-try.fr). For this study we selected four meridional transects that crossed the eddy center.

The first transect (T1; Figure 1a, blue line) traversed the eddy at 4.12 m/s (8 knots) on 3 September in order to obtain current profiles in the upper 750 m by using shipboard acoustic current Doppler profiler (SADCP) measurements from a 75-kHz RDI Ocean Surveyor. The SADCP provided mean current profiles relative to the ship in 16-m bins using the narrowband profiling mode. Data were processed with CODAS software

(https://currents.soest.hawaii.edu/docs/adcp_doc/) and spatially averaged each 0.09° (10 km) as described by Barceló-Llull et al. (2017).

The second transect (T2; Figure 1b) crossed the eddy center between 11 and 14 September to obtain measurements of conductivity-temperature-depth (CTD) and SADCP data. CTD stations along this transect were about five nautical miles (9.3 km) apart and up to 1,000 m in depth. TEOS-10 algorithms were used to calculate potential density anomalies, Brünt-Väisälä frequency, and all related variables (Feistel, 2003, 2008).

Once T2 was completed, the same transect was repeated two more times—hereinafter Transect 3 (T3) and Transect 4 (T4)—at the same cruising speed as T1 (8 knots) in order to obtain continuous vertical sections of the velocity field. Figure 1c shows the time span and the latitudinal range of T2–T4. T2 and T3 extended between 25.1°N and 27.2°N, while T4 was shorter at 25.8–27.2°N. T2 was sampled in 2.8 days (12–14 September), whereas T3 and T4 were completed after 13.3 and 8.8 hr (14 September), respectively.

3. Results

3.1. Velocity Field

The cross-transect (zonal, u) and along-transect (meridional, v) components of the SADCP velocity are represented in Figure 2. The upper panels show vertical sections of the cross-transect velocity for the four transects. The eddy shows a clear anticyclonic circulation with maximum velocity values of ±30–40 cm/s at 100-m depth (Barceló-Llull et al., 2017). Figures 2b–2d also show contours of the potential density anomaly (σ_θ) obtained from T2. The signature of the eddy can be recognized in the density field through the bowl shape of the isopycnals between 100- and 700-m depths, centered in the middle of T2 and T3 and in the southern portion of T4.

As mentioned in the previous section, T2 was sampled within 2.8 days, while T1, T3, and T4 were sampled in 12.8, 13.3, and 8.8 hr, respectively. In the slower speed survey of the eddy (T2), tidal current variability of 12.4 hr period (semidiurnal) is observed as vertical coherent bands of along-transect velocity. The tidal currents can also be identified in the cross-transect component (Figure 2b) but are barely evident because they are masked by the eddy current in this component. The tidal perturbation affects the entire measured water column, consistent with the observations of Siedler and Paul (1991) who showed that the tidal current in this region is dominated by a barotropic mode of about 3–4 cm/s of semimajor axis, in addition to a less energetic low-order (or large vertical length scale) baroclinic mode.

In order to investigate the presence of internal waves in the flow field, the observed horizontal velocity (u,v) was decomposed into a vertical trend (u^t, v^t) and a velocity anomaly (u', v'). The vertical trend was obtained by applying a 350-m low-pass Butterworth filter to vertical profiles of the horizontal velocity (the adjustment of polynomial functions was also applied but did not change the results). The velocity anomaly was obtained by subtracting the vertical trend from the observed velocity profiles. The purpose of this subtraction was to remove the signal of processes with low variability in the vertical, such as the tidal current and the geostrophic signal of the eddy. The resulting along-transect velocity anomaly (v') fields (Figures 2i–2l) reveal, for all four transects, a similar wave-like pattern located just at the eddy center, and stretching from approximately 400-m depth to almost the maximum sampled depth of 725 m. Stronger velocity anomalies in the along- versus cross-transect direction are expected due to polarization of NIWs by the baroclinicity of the eddy (Whitt & Thomas, 2012). The vertical wavelength of the wave packets observed at the four transects is about 200 m, leading to alternating maxima and minima of v' throughout the water column. It is important to note that the anomalies from T4 (Figure 2l) were displaced about a half wavelength (100 m) along the vertical with respect to the anomalies from T3 (Figure 2k). The temporal interval between the T3 and T4 eddy center sampling was 15 hr, very close to half the local inertial period ($T_f = 27.3$ hr at 26°N). In this regard, the observed phase shift between these transects is consistent with those produced by the upward phase velocity associated with a NIW packet that has propagated downward from the mixed layer. Figures 1a and 1b show that the eddy moved about 0.352° (39 km) westward during the 11 days that elapsed between T1 and T4, resulting in typical westward propagation speeds of 4.1 cm/s (Chelton et al., 2011). The observation of amplified wave signals near the base of the eddy in all four transects was an early indication that these NIWs were trapped waves traveling together with the eddy.
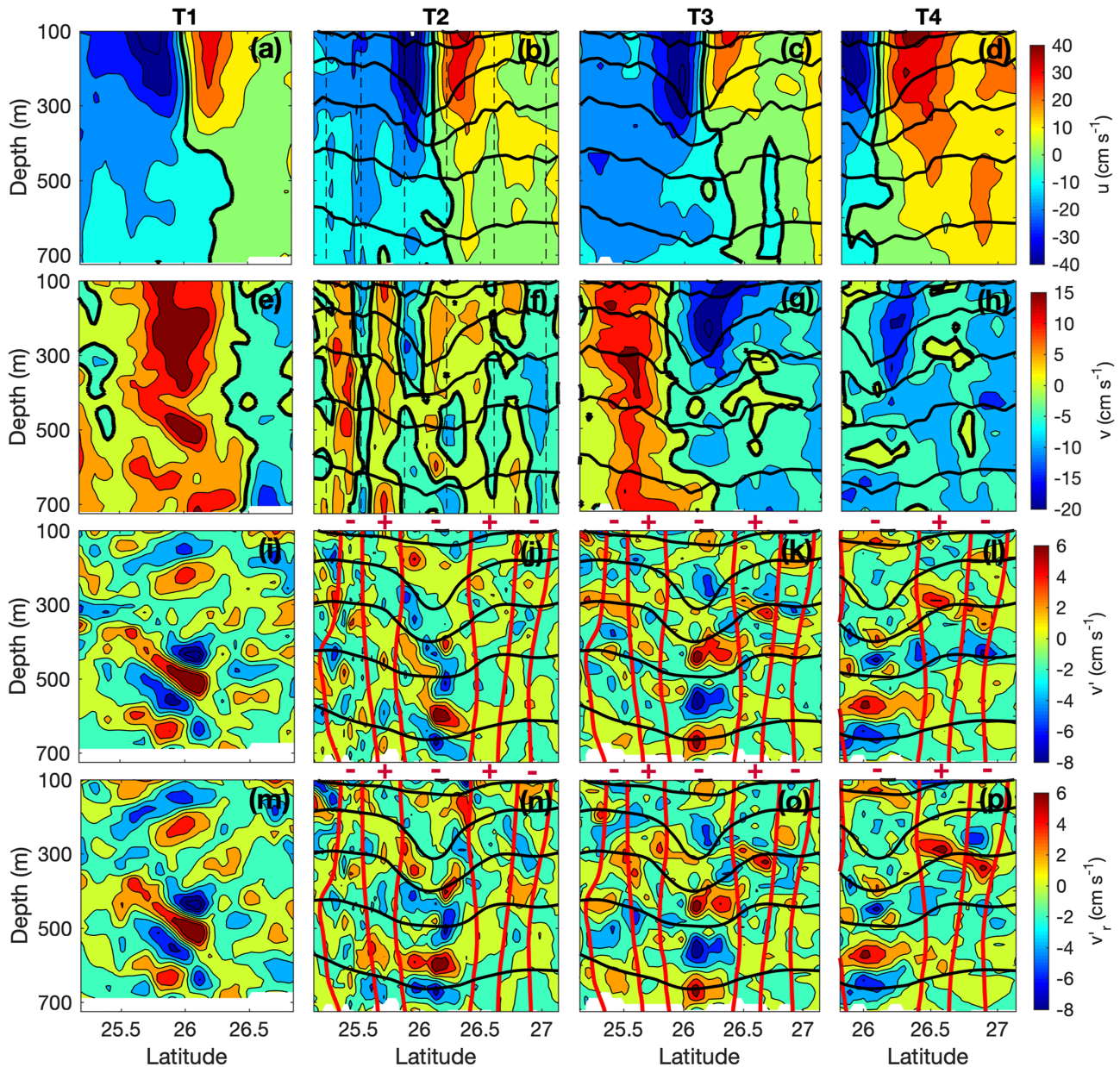
Figure 2. (a–d) SADCP cross-transect (zonal) velocity component (u) at the four transects T1, T2, T3, and T4; (e–h) along-transect (meridional) velocity component (v); (i–l) along-transect velocity anomaly (v'); and (m–p) back-rotated along-transect velocity anomaly (v'_r). Black thick contours indicate isopycnals as obtained from the CTD transect T2 (contour interval of 0.2 kg/m^3 between 26.4 and 27.2 kg/m^3). Dashed vertical lines in (b) and (f) indicate the position of the ship along T2 each 12.4 hr, the period of the main tidal constituent (M2). In (j)–(l) and (n)–(p) the black contours show the smoothed density field used to calculate the cross-transect geostrophic velocity component. Contours of zero geostrophic relative vorticity are superimposed in red. Regions of cyclonic and anticyclonic vorticity are indicated by (+) and (−) symbols, respectively.

The geostrophic velocity relative to 1,000 dbar (u_g, not shown) was computed from the T2 smoothed density field (Butterworth filter; cutoff scale = 0.5°) to reduce the perturbations in the depth of the isopycnals due to tidal and internal wave propagation observed in Figures 2b and 2f (smoothed isopycnals are displayed in Figures 2j–2l and 2n–2p). The vertical component of the geostrophic vorticity was approximated as $\zeta_g = -\partial u_g/\partial y$. As shown in Figures 2j–2l and 2n–2p, a $\zeta_g < 0$ vertical band is found within the core of the eddy, consistent with its anticyclonic nature. At the transitions between the eddy and the surrounding waters the vorticity reverses sign along two vertical bands of positive ζ_g. This vorticity distribution is typical of anticyclonic eddies (e.g., Sangrà et al., 2005); a ring of positive vorticity is generated around the eddy core
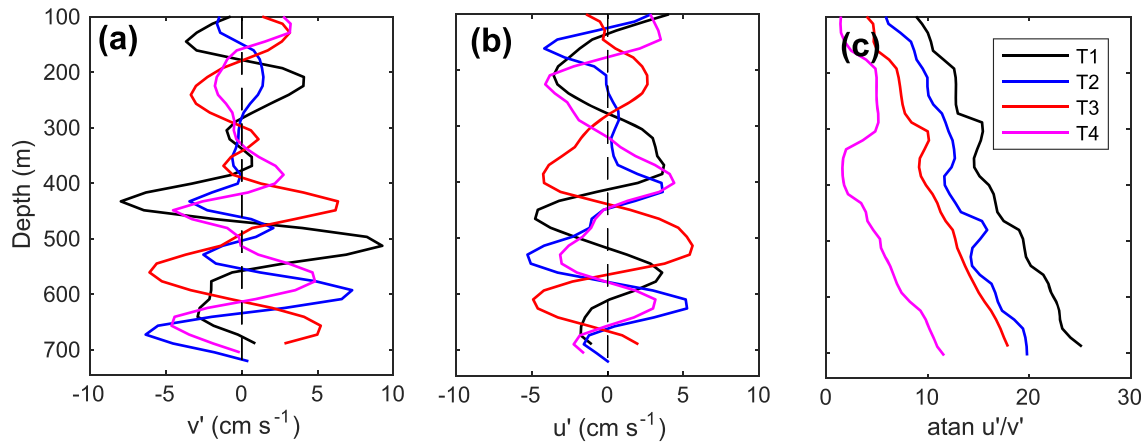
Figure 3. Vertical profiles at the center of the eddy for each transect T1 (black line), T2 (blue line), T3 (red line), and T4 (magenta line) of the (a) along-transect velocity anomaly (v'); (b) cross-transect velocity anomaly (u'); and (c) unwrapped angle in radians of the velocity anomalies (u',v').

due to the decrease of the angular velocity at the edges of the eddy. As expected for NIWs trapped in critical layers, the enhanced wave packets observed near the base of the eddy were confined in the region of anticyclonic vorticity.

Space-time aliasing may occur due to the rotation of the near-inertial currents during long periods of sampling. The aliasing effect is expected to be relatively small for the T1, T3, and T4 velocity fields, as these transects were sampled at shorter times than the inertial period. In contrast, T2 was sampled in 2.8 days, and thus, the wave-like pattern observed is strongly distorted. We can reduce this aliasing by using a complex demodulation known as inertial back rotation (Alford et al., 2013; Leaman & Sandford, 1975). Defining the complex velocity anomaly as $w' = u' + iv'$, we assume that it has a time/space structure given by

$$w'(x, y, z, t) = \widehat{w}(x, y, z)e^{-i\omega(t-t_r)}, \tag{1}$$

that represents a wave packet with spatial structure $\widehat{w}$ rotating clockwise at frequency ω. The structure $\widehat{w}$ is assumed to evolve slowly relative to the inertial period. The reference time t_r is the time at which the vessel passed through the eddy center in each transect. If the wave dominates the spatial structure of the velocity anomaly, then the "back rotation," or multiplication by $e^{i\omega(t-t_r)}$, gives $\widehat{w}(x, y, z)$. Back-rotated velocity anomalies were calculated assuming $\omega = f = 2\pi/T_f = 6.39 \times 10^{-3}$ rad/s. This operation removes the temporal phase propagation that distorts the NIW packet in T2 (Figures 2m–2p).

The phase lines of the wave packet observed near the base of the eddy (500–720 m) in T2–T4 (Figures 2n–2p) are oriented almost horizontally parallel to the isopycnals, as predicted by Whitt and Thomas (2012) and Joyce et al. (2013) for NIWs trapped within critical layers. However, in T1 (Figure 2m) the phases are clearly tilted, suggesting that the wave packet was still propagating downward and approaching the critical layer in this section. The alignment of the phase lines with the isopycnals is not observed in T2–T4 between 350- and 500-m depths, where they are oriented along a different angle (Figures 2n–2p). This observation is also consistent with the theory of Whitt and Thomas (2012) in which the angles tend to be smaller the closer the waves are to the critical layer. In summary, the above results suggest that the NIW amplified signal observed near the base of the eddy in T2–T4 may have come from the downward packet observed at T1 about 7–11 days before, with the additional contribution of NIWs generated later.

The presence of trapped NIWs is also evidenced through a simple inspection of the vertical profiles of the along-transect and cross-transect velocity anomalies at the eddy center (Figure 3). Both u' and v' components show a clear amplified wave-like pattern near the eddy base extending vertically from 400 to almost 720 m (Figures 3a and 3b). The phase angle of the velocity anomalies within this layer indicate a clockwise rotation with increasing depth (Figure 3c). Again, this is consistent with the upward phase velocity (downward group velocity) of NIWs that were generated at the surface (Leaman & Sandford, 1975). The average vertical wavenumber obtained from the four profiles shown in Figure 3c between 400- and 720-m depths

is 0.0315 rad/m, corresponding to a vertical wavelength of 199 m, the same as that observed in the vertical sections of Figure 2.

3.2. Gradient Richardson Number

Ocean turbulent mixing can be generated by shear or Kelvin-Helmholtz instability (e.g., Kundu & Beardsley, 1991) and by convective instability (e.g., Munk, 1981; Thorpe, 1978) in which steep internal waves cause an overturning of the crests. A criterion to determine the stability of stratified shear flows may be obtained in terms of a gradient Richardson number, defined as $Ri = N^2/V_z^2$, where N is the Brunt-Väisälä frequency and $V_z^2 = (\partial u/\partial z)^2 + (\partial v/\partial z)^2$ is the squared vertical shear. Following Abarbanel et al. (1984) and Canuto et al. (2001), we can assume that small-scale mixing due to shear instability is induced when $Ri \leq 1$. The additional effects of the internal wave shear and the coarse vertical resolution of the velocity measurements (16 m in our case) may increase this critical value (Fer et al., 2018; Munk, 1981; Polzin, 1996). In addition, NIWs have the potential to be effective at mixing in the ocean interior as a result of variance at small vertical scales and their great shear/strain ratio (Alford et al., 2016).

To estimate consistent Ri, CTD data were averaged over the same 16-m depth bins as the SADCP data. Brunt-Väisälä frequencies and velocity shear were calculated from CTD and SADCP data, respectively, using central differences. The distribution of N^2, Sh^2, and Ri along T2 is shown in Figures 4a–4c, respectively. A pycnostad layer is revealed by the separation of the isopycnals between approximately 150- and 300-m depths. This nearly homogeneous interior layer is also evident in the vertical section of N^2 as a patch of low stratification (Figure 4a). The comparison between V_z^2 (Figure 4b) and the shear calculated only with the velocity anomaly ($V_z'^2$, Figure 4d) shows that the trapping of NIWs near the eddy base (Figure 2) generates the maximum values of V_z^2 observed from 350 m to the maximum sampled depth. There are also two relatively high shear regions at about 200–300 m on both sides of the eddy center that are related to the maximum velocities at the edges of the eddy core. Between 350- and 720-m depths, the Richardson number is mainly determined by the shear generated by the velocity anomalies (Figures 4b–4e) and reaches values lower than 1 between 500- and 700-m depths (Figure 4c), suggesting that mixing events were triggered by shear instability near the base of the eddy.

3.3. Strain Variance and Parameterization of Turbulent Kinetic Energy Dissipation Rate

The density profiles of T2 were divided into 200-m half-overlapping segments of 2-m resolution beginning at the bottom of each profile. Internal wave strain was estimated from Brunt-Väisälä frequency as $\xi_z = (N^2 - N_{\text{fit}}^2)/\overline{N^2}$, where $\overline{N^2}$ is the squared Brunt-Väisälä frequency averaged over a depth segment and N_{fit}^2 is a quadratic fit of N^2 in each segment (Pasquet et al., 2016; Whalen et al., 2015). Then, the strain variance ξ_z^2 was obtained by integrating the Fourier transformation of ξ_z. The integration range was limited to vertical wavelengths of 100 and 40 m. With these limits the condition $\xi_z^2 \leq 0.2$, necessary to avoid oversaturation of the spectrum that could underestimate the variance (Gargett, 1990), was satisfied. Following the procedure of Whalen et al. (2012, 2015) the segments affected by areas of low stratification (in our case the surface mixed layer and the pycnostad) that reduce the accuracy of the estimations, were removed. Figure 4f shows that enhanced strain variances of the order of $10^{-0.8}$–$10^{-1.2}$ (Figure 4f) are obtained near the base of the eddy but more widespread in the horizontal than the shear variance.

Parameterizations based on the mixing generated by the breaking of internal waves by convective instability (Gregg, 1989; Polzin et al., 1995) have been widely applied to and contrasted with microstructure data over the last two decades (e.g., Gregg et al., 2003; Kunze et al., 2006; Naveira-Garabato et al., 2004; Pasquet et al., 2016; Polzin et al., 2014; Whalen et al., 2012; Whalen et al., 2015; Wu et al., 2011). These parameterizations rely on the assumption that the rate at which wave breaking dissipates energy roughly equals the rate at which the energy is transferred from large to small scales. Such equivalence allows the dissipation rate to be expressed in terms of strain variance as

$$\epsilon = \epsilon_0 \frac{\overline{N^2}}{N_0^2} \frac{\langle \xi_z^2 \rangle^2}{\langle \xi_{z\text{GM}}^2 \rangle^2} h(R_\omega) L(f, N), \tag{2}$$

where $\epsilon_0 = 6.73 \times 10^{-10}$ W/kg is the canonical Garrett and Munk (GM hereafter) dissipation rate at 30° of
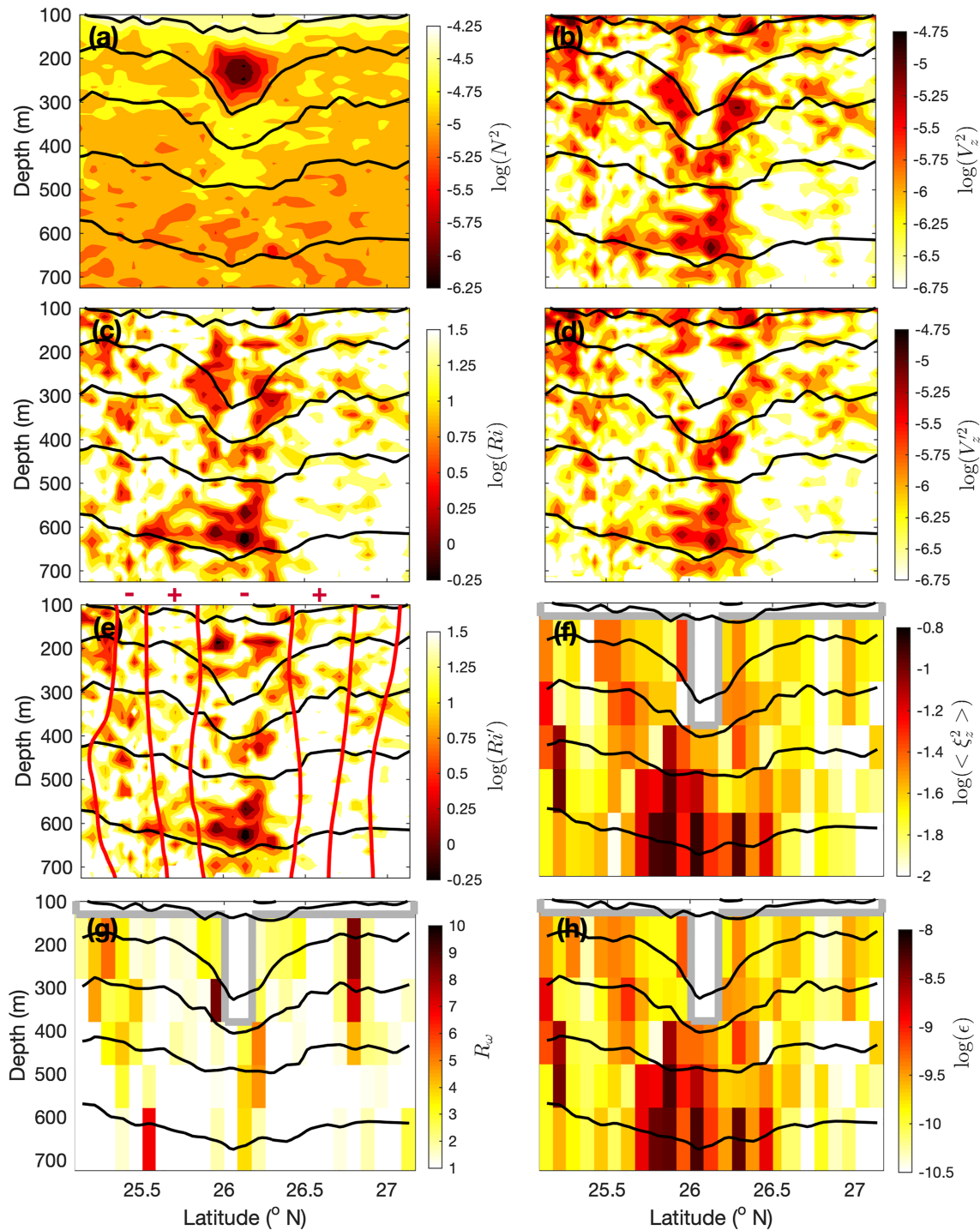
Figure 4. Vertical sections along T2 of the logarithm of the (a) squared Brünt-Väisälä frequency (N^2) computed from density; (b) squared vertical shear (V_z^2) obtained with SADCP velocity; (c) gradient Richardson number (Ri) inferred with V_z^2; (d) squared vertical shear computed with the velocity anomaly ($V_z'^2$); (e) Richardson number inferred with $V_z'^2$ (Ri'); (f) strain variance between wavelengths of 40 and 100 m ($\langle \xi_z^2 \rangle$) computed in 200-m half-overlapping segments; (g) shear-to-strain ratios (R_ω) calculated using equation (4); and (h) the corresponding computed logarithm of ϵ. Black thick contours indicate isopycnals as obtained from the CTD transect T2 (contour interval of 0.2 kg/m^3 between 26.4 and 27.2 kg/m^3). Contours of zero geostrophic relative vorticity are superimposed in red in (g). Regions of cyclonic and anticyclonic vorticity are indicated by (+) and (−) symbols, respectively. Gray thick lines in (f)–(h) enclose the removed segments affected by areas of low stratification (surface mixed layer and pycnostad).

latitude for $N = N_0$ (Garrett & Munk, 1979), $N_0 = 5.24 \times 10^{-3}$ rad/s and $\xi^2_{z\text{GM}}$ represent the observed and GM strain variance. The function $L(f,N)$ accounts for the latitudinal dependence of the internal wave field and $h(R_\omega)$ accounts for the dependence on the shear-to-strain ratio (R_ω) and is defined as

$$h(R_\omega) = \frac{1}{6\sqrt{2}} \frac{R_\omega(R_\omega + 1)}{\sqrt{R_\omega - 1}},$$

(3)

where R_ω is normally set to 3 (the GM value) when no velocity data are available (e.g., Whalen et al., 2012; Wu et al., 2011).

The main limitation of the above parameterization is the assumption that R_ω is constant. However, the density and velocity profiles measured along T2 allowed us to estimate the variation of this parameter as (Polzin et al., 1995):

$$R_\omega = \frac{\langle V_z^2 \rangle}{\overline{N}^2 \langle \xi_z^2 \rangle}$$

(4)

To obtain shear variances V_z^2, the SADCP vertical shear profiles were interpolated each 2 m to match the Brunt-Väisälä frequency depths. The resulting profiles were Fourier transformed over the same 200-m half-overlapping segments as the strain profiles and integrated within the same wavenumber limits. These shear spectra were corrected for loss of variance due to range averaging, finite differencing, and interpolation as detailed in Polzin et al. (2002). The results show relatively high values ($R_\omega > 3$) within three vertical bands located at the center and edges of the eddy (Figure 4g) that roughly coincide with the three negative vorticity ridges observed in Figure 2. As pointed out by Polzin et al. (1995), the shear-to-strain ratio can be considered a measure of the aspect ratio (which is related in turn with the frequency content) of the internal wave field. In our case, a high R_ω implies that the mean internal wave properties in the analyzed 200-m segments are closer to near-inertial values (predominantly horizontal motions and frequencies near to f) than a low R_ω, which implies the opposite (predominantly vertical motions and frequencies closer to N). A relationship between shear-to-strain ratios and vorticities is consistent with the theories of Kunze (1985) and Young and Ben Jelloul (1997), which show that near-inertial energy is attracted to regions of negative vorticity and expelled from regions of positive vorticity. The logarithm of dissipation rates calculated with variable R_ω (Figure 4h) shows enhanced dissipation rates of the order of 10^{-8}–10^{-9} W/kg near the base of the eddy, in comparison with low dissipation rates of order 10^{-10}–10^{-11} W/kg in the surrounding waters.

3.4. Winds

Both the smoothed daily winds from the ASCAT scatterometers (Figure 5a, black line) and the hourly averaged winds from the meteorological station mounted on the ship (Figure 5a, blue line) show that the wind speed was low to moderate (<8 m/s) throughout the cruise. In addition, the ASCAT data evidence that the wind intensity in the study area was higher before (between 4 and 8 m/s) than during (between 1 and 5 m/s) the cruise. The wind speed fluctuations observed with the meteorological station were more important between 1 and 8 September (during T1) than between 9 and 16 September (during T2–T4). The northward and eastward components of the wind velocity (Figure 5b) highlight this relatively high variability during the first half of the survey. The higher wind speed before the eddy sampling and the wind speed variability during T1 may explain why the current velocity anomaly signal is stronger in T1 than in T2–T4 (Figures 2m–2p and 3a and 3b). Finally, Figure 5c shows that the survey was carried out during the month with the weakest winds of 2014 (red line), which usually occurs in September, as demonstrated by the climatological wind speed from the ASCAT scatterometers (blue line)

4. Discussion

The analysis of cross-eddy sections of density and SADCP data shows the presence of NIW packets with vertical wavelengths of 200 m near the base of the anticyclonic eddy. The following properties demonstrate that the observed packets are trapped waves within the eddy: (a) The NIWs were observed within the region of anticyclonic vorticity, which is consistent with the NIWs trapping theory (Balmforth et al., 1998; Kunze, 1985; Young & Ben Jelloul, 1997); (b) the wave phases of the packets in Transects 2, 3, and 4 are aligned with
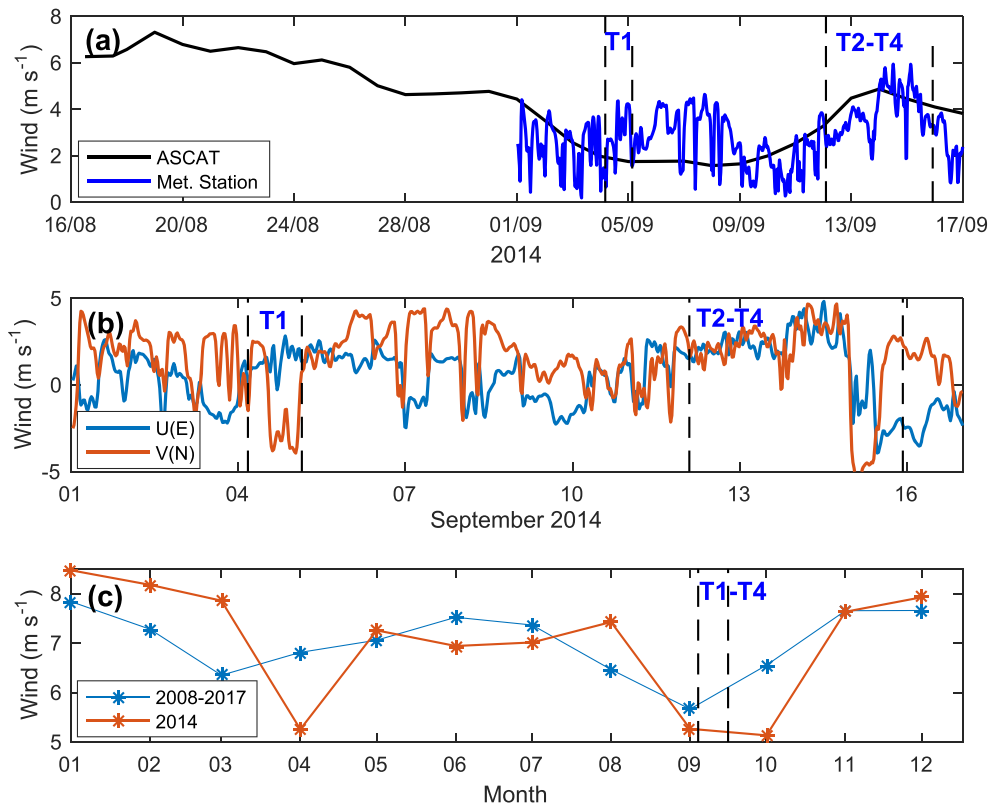
Figure 5. (a) Smoothed daily winds from the ASCAT scatterometers (black line) on board METOP-A and METOP-B satellites (http://marine.copernicus.eu) and hourly averaged wind speed recorded by the meteorological station mounted on the ship (blue line). (b) Eastward (U) and northward (V) components of the wind from the meteorological station. (c) Monthly averaged winds for the period 2008–2017 (blue line) and for 2014 (red line) calculated from ASCAT scatterometers.

isopycnals between 500 and 720 m, which is an indication that NIWs are near their critical layer (Joyce et al., 2013; Whitt & Thomas, 2012); (c) velocity anomalies at the center of the eddy show a clear amplified wave-like pattern near the eddy base and a clockwise rotation with increasing depth indicating downward propagation (Leaman & Sandford, 1975; Whitt & Thomas, 2012).

Fine-scale Richardson numbers are not considered a good estimator of where the mixing occurs, but they have been considered as a useful proxy of turbulence production in the oceans (e.g., Alford & Gregg, 2001; Alford & Pinkel, 2000; Dillon, 1982; Fer et al., 2018; Kitade et al., 2003; Polzin, 1996). In addition, low fine-scale Ri associated with NIWs has been frequently measured in the ocean interior as a result of variance at relatively small vertical scales and their great shear/strain ratio (e.g., Alford & Gregg, 2001; Avicola et al., 2007; Fer, 2014; Fer et al., 2018; Hebert & Moum, 1994; Pallàs-Sanz, Candela, Sheinbaum, Ochoa, & Jouanno, 2016). In all these works, shear at scales unresolved by the acoustic current Doppler profiler was assumed to lower the total Richardson number enough to trigger shear instability. Our results, obtained with a vertical resolution of 16 m, show Ri near 1 just at the region where trapped NIWs are detected, which imply a significant probability of turbulence generation.

Our results also show enhanced strain variance near the base of the eddy (Figure 4f). Strain variance are usually associated to waves with vertical scales lower than NIWs (Kunze et al., 2006). As theoretically explained by Kunze et al. (1995), the trapped near-inertial energy cannot concentrate infinitely at the critical layer, and it must be a sink for near-inertial energy: transference to the mean flow, transference to untrapped smaller-scale waves, and instability of the growing NIW's shear, triggering turbulence production and mixing. In turn, the untrapped waves must transfer energy toward smaller-scale waves that subsequently break into turbulence. This energy transference from large to small scales is indeed the basic assumption of the parameterization of turbulent kinetic energy dissipation rate used to estimate the turbulence from fine-

scale strain variance (e.g., Polzin et al., 2014; Whalen et al., 2015). It is important to keep in mind that this parameterization rely on the assumption that the wave field is statistically steady (Gregg et al., 2003). In this case, the rate at which wave breaking dissipates energy roughly equals the rate at which the energy is transferred from large to small scales. To fulfill this condition, the trapped near-inertial energy observed in our experiment should vary slowly over time. The observation of NIW packets near the eddy base at two different stages of the survey separated by 10 days suggest that our findings may be common, but this does not ensure the statistically steady assumption. However, we can use the parameterization as a turbulence proxy, not to quantify it. In this sense, the region of enhanced strain variance of the order of $10^{-0.8}$–$10^{-1.2}$ (and consequently increased dissipation rates) found near the place where wave packet was observed (Figure 2d) strongly suggest, in addition to $Ri \leq 1$, the generation of turbulence associated with trapped NIW energy near a critical layer.

Another remarkable result is that relatively low Ri values are observed between 300- and 720-m depths within the three vertical bands located at the center and edges of the eddy that roughly coincide with three negative vorticity ridges (Figure 4e). These ridges also contain high shear-to-strain ratios ($R_\omega > 3$) implying that the mean internal wave properties are closer to near-inertial values. This result is consistent with the theories of Kunze (1985) and Young and Ben Jelloul (1997), which show that near-inertial energy is attracted to regions of negative vorticity and expelled from regions of positive vorticity. It also provides further evidence that the distribution of Ri in this study is largely determined by NIWs.

We observed NIW packets near the eddy base at two different stages of the survey separated by 10 days. NIWs are generated by variable wind forcing at the ocean surface (e.g., Pollard & Millard, 1970; Chen et al., 2015), with the changes being generally higher during strong wind events (e.g., Alford et al., 2016; Pallàs-Sanz, Candela, Sheinbaum, Ochoa, & Jouanno, 2016). As our experiment took place during a period of the year with low to moderate winds, we suggest that the NIW trapping and the enhancement of deep turbulence during the PUMP survey were not isolated events but may be common in other similar anticyclonic eddies of the Canary Eddy Corridor generated throughout the year.

5. Conclusions

During the PUMP experiment (Barceló-Llull et al., 2017) we sampled a westward propagating long-lived anticyclonic eddy of the Canary Eddy Corridor with four meridional transects that crossed the eddy center. The northeasterly winds of low to moderate intensity that blew during and before the survey had characteristics of late summer trade winds. Our observations provide robust evidence for the trapping of NIW packets of amplitude between 5 and 10 cm/s with vertical wavelengths of about 200 m near the base of the eddy. The observed upward phase propagation (downward energy propagation) strongly suggests that the NIWs were generated at the surface. Gradient Richardson numbers ≤ 1, strain variance of the order of $10^{-0.8}$–$10^{-1.2}$ and increased parameterized turbulent dissipation rates reveal that these trapped NIWs probably enhanced the turbulence near the base of the eddy from about 400-m depth to almost the maximum sampled depth of 725 m. The observation of trapped NIW packets at two different stages of the survey, which took place during the month with the weakest winds of 2014, suggests that the trapping of NIWs may not be an isolated event occurring during the PUMP survey but may be common in other similar anticyclonic eddies of the Canary Eddy Corridor. Hence, anticyclonic mesoscale eddies of the Canary Eddy Corridor and other major pathways for long-lived mesoscale eddies in the World Ocean (Chelton et al., 2007, 2011) may act as open-ocean deep mixing structures as they propagate to the west. In addition, our findings indicate that further microstructure studies and high-resolution sampling within open-ocean mesoscale eddies during normal atmospheric conditions are necessary to quantify the energetics of these wave mean flow interactions and their impacts at global and regional scales.

References

Abarbanel, H. D., Holm, D. D., Marsden, J. E., & Ratiu, T. (1984). Richardson number criterion for the nonlinear stability of three-dimensional stratified flow. *Physical Review Letter*, *52*(26), 2352.

Alford, M. H. (2003). Redistribution of energy available for ocean mixing by long-range propagation of internal waves. *Nature*, *423*(6936), 159–162. https://doi.org/10.1038/nature01628

Alford, M. H., & Gregg, M. C. (2001). Near-inertial mixing: Modulation of shear, strain and microstructure at low latitude. *Journal Geophysical Research*, *106*, 16947–16968. https://doi.org/10.1029/2000JC000370

Alford, M. H., MacKinnon, J. A., Simmons, H. L., & Nash, J. D. (2016). Near-inertial internal gravity waves in the ocean. *Annual Review of Marine Science*, *8*, 95–123. https://doi.org/10.1146/annurev-marine-010814-015746

Alford, M. H., & Pinkel, R. (2000). Observations of overturning in the thermocline: The context of ocean mixing. *Journal of Physical Oceanography*, *30*(5), 805–832. https://doi.org/10.1175/1520-0485(2000)030<0805:OOOITT>2.0.CO;2

Alford, M. H., Shcherbina, A. Y., & Gregg, M. C. (2013). Observations of near-inertial internal gravity waves radiating from a frontal jet. *Journal of Physical Oceanography*, *43*(6), 1225–1239. https://doi.org/10.1175/JPO-D-12-0146.1

Anderson, D. L. T., & Gill, A. E. (1979). Beta dispersion of inertial waves. *Journal of Geophysical Research*, *84*, 1836–1842. https://doi.org/10.1029/JC084iC04p01836

Avicola, G. S., Moum, J. N., Perlin, A., & Levine, M. D. (2007). Enhanced turbulence due to the superposition of internal gravity waves and a coastal upwelling jet. *Journal of Geophysical Research*, *112*, C06024. https://doi.org/10.1029/2006JC003831

Balmforth, N. J., Llewellyn Smith, S. G., & Young, W. R. (1998). Enhanced dispersion of near-inertial waves in an idealized geostrophic flow. *Journal of Marine Research*, *56*, 1–40.

Barceló-Llull, B., Sangrà, P., Pallàs-Sanz, E., Barton, E. D., Estrada-Allis, S. N., Martínez-Marrero, A., et al. (2017). Anatomy of a subtropical intrathermocline eddy. *Deep Sea Research I*, *124*, 126–139. https://doi.org/10.1016/j.dsr.2017.03.012

Canuto, V. M., Howard, A., Cheng, Y., & Dubovikov, M. S. (2001). Ocean turbulence. Part I: One-point closure model-momentum and heat vertical diffusivities. *Journal of Physical Oceanography*, *31*, 1413–1426. https://doi.org/10.1175/1520-0485(2001)031%3C1413:OTPIOP%3E2.0.CO;2

Chelton, D. B., Schlax, M. G., & Samelson, R. M. (2011). Global observations of nonlinear mesoscale eddies. *Progress in Oceanography*, *91*, 167–216.

Chelton, D. B., Schlax, M. G., Samelson, R. M., & de Szoeke, R. A. (2007). Global observations of large oceanic eddies. *Geophysical Research Letters*, *34*, L15606. https://doi.org/10.1029/2007GL030812

Chen, S., Polton, J. A., Hu, J., & Xing, J. (2015). Local inertial oscillations in the surface ocean generated by time-varying winds. *Ocean Dynamics*, *65*(12), 1633–1641. https://doi.org/10.1007/s10236-015-0899-6

Cuypers, Y., Bouruet-Aubertot, P., Marec, C., & Fuda, J.-L. (2012). Characterization of turbulence from a fine-scale parameterization and microstructure measurements in the Mediterranean Sea during the BOUM experiment. *Biogeosciences*, *9*(8), 3131–3149. https://doi.org/10.5194/bg-9-3131-2012

Danioux, E., & Klein, P. (2008). A resonance mechanism leading to wind-forced motions with a 2*f* frequency. *Journal of Physical Oceanography.*, *38*(10), 2322–2329. https://doi.org/10.1175/2008JPO3821.1

Danioux, E., Vanneste, J., & Bühler, O. (2015). On the concentration of near-inertial waves in anticyclones. *Journal of Fluid Mechanics*, *773*(R2). https://doi.org/10.1017/jfm.2015.252

D'Asaro, E. A., Eriksen, C., Levine, D., Niiler, P., Paulson, A., & Van Meurs, P. (1995). Upper-ocean inertial currents forced by a strong storm. Part I: Data and comparisons with linear theory. *Journal of Physical Oceanography*, *25*, 2909–2936.

Dillon, T. M. (1982). Vertical overturns: A comparison of Thorpe and Ozmidov length scales. *Journal of Geophysical Research*, *87*(C12), 9601–9613. https://doi.org/10.1029/JC087iC12p09601

Feistel, R. (2003). A new extended Gibbs thermodynamic potential of seawater. *Progress in Oceanography*, *58*(1), 43–114. https://doi.org/10.1016/S0079-6611(03)00088-0

Feistel, R. (2008). A Gibbs function for seawater thermodynamics for −6 to 80 °C and salinity up to 120 g kg^{-1}. *Deep Sea Research Part I: Oceanographic Research Papers*, *55*(12), 1639–1671. https://doi.org/10.1016/j.dsr.2008.07.004

Fer, I. (2014). Near-inertial mixing in the central Arctic Ocean. *Journal of Physical Oceanography*, *44*(8), 2031–2049. https://doi.org/10.1175/JPO-D-13-0133.1

Fer, I., Bosse, A., Ferron, B., & Bouruet-Aubertot, P. (2018). The dissipation of kinetic energy in the Lofoten Basin Eddy. *Journal of Physical Oceanography*, *48*, 1299–1316. https://doi.org/10.1175/JPO-D-17-0244.1

Gargett, A. E. (1990). Do we really know how to scale the turbulent kinetic energy dissipation rate due to breaking of oceanic internal waves? *Journal of Geophysical Research*, *95*, 15,971–15,974. https://doi.org/10.1029/JC095iC09p15971

Garrett, C. (2001). What is the "near-inertial" band and why is it different from the rest of the internal wave spectrum? *Journal of Physical Oceanography*, *31*, 962–971.

Garrett, C. J. R., & Munk, W. H. (1979). Internal waves in the ocean. *Annual Review of Fluid Mechanics*, *92*, 339–369.

Gregg, M. C. (1989). Scaling turbulent dissipation in the thermocline. *Journal of Geophysical Research*, *94*(C7), 9686–9698. https://doi.org/10.1029/JC094iC07p09686

Gregg, M. C., Sanford, T. B., & Winkel, D. P. (2003). Reduced mixing from the breaking of internal waves in equatorial waters. *Nature*, *422*(6931), 513–515. https://doi.org/10.1038/nature01507

Hebert, D., & Moum, J. (1994). Decay of a near-inertial wave. *Journal of Physical Oceanography*, *24*, 2334–2351.

Joyce, T. M., Toole, J. M., Klein, P., & Thomas, L. N. (2013). A near-inertial mode observed within a Gulf Stream warm-core ring. *Journal of Geophysical Research: Oceans*, *118*, 1797–1806. https://doi.org/10.1002/jgrc.20141

Karstensen, J., Schütte, F., Pietri, A., Krahmann, G., Fiedler, B., Grundle, D., et al. (2017). Upwelling and isolation in oxygen-depleted anticyclonic modewater eddies and implications for nitrate cycling. *Biogeosciences*, *14*, 2167–2181. https://doi.org/10.5194/bg-14-2167-2017

Kawaguchi, Y., Nishino, S., Inoue, J., Maeno, K., Takeda, H., & Oshima, K. (2016). Enhanced diapycnal mixing due to near-inertial internal waves propagating through an anticyclonic eddy in the ice-free Chukchi Plateau. *Journal of Physical Oceanography*, *46*, 2457–2481. https://doi.org/10.1175/JPO-D-15-0150.1

Kitade, Y., Matsuyama, M., & Yoshida, J. (2003). Distribution of overturn induced by internal tides and Thorpe scale in Uchiura Bay. *Journal of Oceanography*, *59*, 845. https://doi.org/10.1023/B:JOCE.0000009575.29339.35

Kundu, P. K., & Beardsley, R. C. (1991). Evidence of a critical Richardson number in moored measurements during the upwelling season off Northern California. *Journal of Geophysical Research*, *96*, 4855–4868. https://doi.org/10.1029/90JC02108

Kunze, E. (1985). Near-inertial wave propagation in geostrophic shear. *Journal of Physical Oceanography*, *15*, 544–565.

Kunze, E., Firing, E., Hummon, J. M., Chereskin, T. K., & Thurnherr, A. M. (2006). Global abyssal mixing inferred from lowered ADCP shear and CTD strain profiles. *Journal of Physical Oceanography*, *36*, 1553–1576.

Kunze, E., Schmitt, R. W., & Toole, J. M. (1995). The energy balance in a warm- core ring's near-inertial critical layer. *Journal of Physical Oceanography*, *25*, 942–957. https://doi.org/10.1175/1520-0485(1995)025<0942:TEBIAW>2.0.CO;2

Leaman, K. D., & Sandford, T. B. (1975). Vertical energy propagation of inertial waves: A vector spectral analysis of velocity profiles. *Journal of Geophysical Research*, *80*, 1975–1978. https://doi.org/10.1029/JC080i015p01975

Lee, D., & Niiler, P. P. (1998). The inertial chimney: The near-inertial energy drainage from the ocean surface to the deep layer. *Journal of Geophysical Research*, *103*, 7579–7591. https://doi.org/10.1029/97JC03200

Lueck, R., & Osborn, T. (1986). The dissipation of kinetic energy in a warm-core ring. *Journal of Geophysical Research*, *91*(C1), 803–818. https://doi.org/10.1029/JC091iC01p00803

Munk, W. (1981). Internal waves and small-scale processes. In B. A. Warren & C. Wunsch (Eds.), *Evolution of physical oceanography* (pp. 264–291). Cambridge: MIT Press.

Munk, W., & Wunsch, C. (1998). Abyssal recipes II: Energetics of tidal and wind mixing. *Deep Sea Research Part I: Oceanographic Research Papers*, *45*(12), 1977–2010. https://doi.org/10.1016/S0967-0637(98)00070-3

Naveira-Garabato, A. C., Oliver, K. I. C., Watson, A. J., & Messias, M. J. (2004). Turbulent diapycnal mixing in the Nordic seas. *Journal of Geophysical Research*, *109*, C12010. https://doi.org/10.1029/2004JC002411

Pallàs-Sanz, E., Candela, J., Sheinbaum, J., & Ochoa, J. (2016). Mooring observations of the near-inertial wave wake of Hurricane Ida (2009). *Dynamics of Atmospheres and Oceans*, *76*, 325–344. https://doi.org/10.1016/j.dynatmoce.2016.05.003

Pallàs-Sanz, E., Candela, J., Sheinbaum, J., Ochoa, J., & Jouanno, J. (2016). Trapping of the near-inertial wave wakes of two consecutive hurricanes in the Loop Current. *Journal of Geophysical Research: Oceans*, *121*, 7431–7454. https://doi.org/10.1002/2015JC011592

Pasquet, S., Bouruet-Aubertot, P., Reverdin, G., Turnherr, A., & St. Laurent, L. (2016). Finescale parameterizations of energy dissipation in a region of strong internal tides and sheared flow, the Lucky-Strike segment of the Mid-Atlantic Ridge. *Deep Sea Research I*, *112*, 79–93. https://doi.org/10.1016/j.dsr.2015.12.016

Pollard, R. T., & Millard, R. C. Jr. (1970). Comparison between observed and simulated wind-generated inertial oscillations. *Deep Sea Research and Oceanographic Abstracts*, *17*(4), 813–816. https://doi.org/10.1016/0011-7471(70)90043-4

Polzin, K. (1996). Statistics of the Richardson number: Mixing models and finestructure. *Journal of Physical Oceanography*, *26*, 1409–1425.

Polzin, K. L., Kunze, E., Hummon, J., & Firing, E. (2002). The finescale response of lowered ADCP velocity profilers. *Journal of Atmospheric and Oceanic Technology*, *19*, 205–224.

Polzin, K. L., Naveira Garabato, A. C., Huussen, T. N., Sloyan, B. M., & Waterman, S. (2014). Finescale parameterizations of turbulent dissipation. *Journal of Geophysical Research: Oceans*, *119*, 1383–1419. https://doi.org/10.1002/2013JC008979

Polzin, K. L., Toole, J. M., & Schmitt, R. W. (1995). Finescale parameterizations of turbulent dissipation. *Journal of Physical Oceanography*, *25*(3), 306–328.

Sangrà, P., Pascual, A., Rodríguez-Santana, A., Machín, F., Mason, E., McWilliams, J. C., et al. (2009). The Canary Eddy Corridor: A major pathway for long-lived eddies in the subtropical North Atlantic. *Deep-Sea Research I*, *56*, 2100–2114. https://doi.org/10.1016/j.dsr.2009.08.008

Sangrà, P., Pelegrí, J. L., Hernández-Guerra, A., Arregui, I., Martín, J. M., Marrero-Díaz, A., et al. (2005). Life history of an anticyclonic eddy. *Journal of Geophysical Research*, *110*, C03021. https://doi.org/10.1029/2004JC002526

Siedler, G., & Paul, U. (1991). Barotropic and baroclinic tidal currents in the eastern basins of the North Atlantic. *Journal of Geophysical Research*, *96*, 22259–22271. https://doi.org/10.1029/91JC02319

St. Laurent, L., & Garrett, C. (2002). The role of internal tides in mixing the deep ocean. *Journal of Physical Oceanography*, *32*, 2882–2899.

Thorpe, S. A. (1978). On the shape and breaking of finite amplitude internal gravity waves in a shear flow. *Journal of Fluid Mechanics*, *85*, 7–31.

Waterhouse, A. F., MacKinnon, J. A., Nash, J. D., Alford, M. H., & Kunze, E. (2014). Global patterns of diapycnal mixing from measurements of the turbulent dissipation rate. *Journal of Physical Oceanography*, *44*, 1854–1872.

Whalen, C. B., MacKinnon, J. A., Talley, L. D., & Waterhouse, A. F. (2015). Estimating the mean diapycnal mixing using a finescale strain parameterization. *Journal of Physical Oceanography*, *45*, 1174–1188.

Whalen, C. B., Talley, L. D., & Mackinnon, J. A. (2012). Spatial and temporal variability of global ocean mixing inferred from Argo profiles. *Geophysical Research Letters*, *39*, L18612. https://doi.org/10.1029/2012GL053196

Whitt, D. B., & Thomas, L. N. (2012). Near-inertial waves in strongly baroclinic currents. *Journal of Physical Oceanography*, *43*, 706–725.

Wu, L., Jing, Z., Riser, S., & Visbeck, M. (2011). Seasonal and spatial variations of Southern Ocean diapycnal mixing from Argo profiling floats. *Nature Geoscience*, *4*, 363–366. https://doi.org/10.1038/NGEO1156

Wunsch, C., & Ferrari, R. (2004). Vertical mixing, energy, and the general circulation of the oceans. *Annual Review in Fluid Mechanics*, *36*, 281–314.

Young, W. R., & Ben Jelloul, M. (1997). Propagation of near-inertial oscillations through a geostrophic flow. *Journal of Marine Research*, *55*, 735–766.

Zhai, X., Greatbatch, R. J., & Eden, C. (2007). Spreading of near-inertial energy in a 1/12° model of the North Atlantic Ocean. *Geophysical Research Letters*, *34*, L10609. https://doi.org/10.1029/2007GL029895

Zhai, X., Greatbatch, R. J., & Zhao, J. (2005). Enhanced vertical propagation of storm-induced near-inertial energy in an eddying ocean channel model. *Geophysical Research Letters*, *32*, L18602. https://doi.org/10.1029/2005GL023643